


## Geometric entanglement in integer quantum Hall states

Benoit Sirois <sup>1,2</sup>, Lucie Maude Fournier,<sup>2</sup> Julien Leduc,<sup>2</sup> and William Witczak-Krempa<sup>2,3,4</sup>

<sup>1</sup>*Theoretical Physics, Oxford University, 1 Keble Road, Oxford OX1 3NP, United Kingdom*

<sup>2</sup>*Département de Physique, Université de Montréal, Montréal, Québec, Canada H3C 3J7*

<sup>3</sup>*Centre de Recherches Mathématiques, Université de Montréal; P.O. Box 6128, Centre-ville Station, Montréal (Québec), Canada H3C 3J7*

<sup>4</sup>*Regroupement Québécois sur les Matériaux de Pointe (RQMP)*



(Received 12 September 2020; revised 24 November 2020; accepted 24 February 2021; published 9 March 2021)

We study the quantum entanglement structure of integer quantum Hall states via the reduced density matrix of spatial subregions. In particular, we examine the eigenstates, spectrum, and entanglement entropy (EE) of the density matrix for various ground and excited states, with or without mass anisotropy. We focus on an important class of regions that contain sharp corners or cusps, leading to a geometric angle-dependent contribution to the EE. We unravel surprising relations by comparing this corner term at different fillings. We further find that the corner term, when properly normalized, has nearly the same angle dependence as numerous conformal field theories (CFTs) in two spatial dimensions, which hints at a broader structure. In fact, the Hall corner term is found to obey bounds that were previously obtained for CFTs. In addition, the low-lying entanglement spectrum and the corresponding eigenfunctions reveal “excitations” localized near corners. Finally, we present an outlook for fractional quantum Hall states.

DOI: [10.1103/PhysRevB.103.115115](https://doi.org/10.1103/PhysRevB.103.115115)

### I. INTRODUCTION

Restricting observations to a spatial subregion of a quantum system, such as a cold two-dimensional electron gas (2DEG), gives information about the entire system due to the presence of entanglement. Rather than studying specific observables localized in the region, one can examine the reduced density matrix, which is obtained by taking the full density matrix and tracing out degrees of freedom outside the region of interest. Due to the large amount of information stored in that reduced density matrix, it is often advantageous to study parts of it, such as subset of its eigenstates, spectrum (called the entanglement spectrum), and more simply, the entanglement entropy (EE). The latter is a positive number that, heuristically speaking, quantifies how much entanglement exists between a region and its complement.<sup>1</sup>

The entanglement spectrum and EE have been particularly useful in revealing the topological properties of two-dimensional (2D) quantum systems [1–5], such as quantum Hall states. Indeed, the topological EE, which depends on the topology of the subregion not its geometry, gives insight about the anyons present in a topologically ordered state. The shape or geometrical dependence of the reduced density matrix also contains rich information about the system. The geometrical aspects have been particularly studied for the ground states of gapless quantum systems, such as conformal field theories, through the EE [5–19]. In this work, we analyze the geometrical properties of the reduced density matrix for a particularly simple class of topological states,

the integer quantum Hall (IQH) states. Although idealized IQH wave functions represent noninteracting fermions, they nevertheless possess a rich spatial entanglement structure. As we shall show, certain entanglement properties of IQH states closely resemble those of strongly interacting quantum critical systems in two spatial dimensions.

#### A. Entanglement entropy in quantum Hall states

More precisely, the von Neumann EE of a subregion  $A$  in a state described by a density matrix  $\rho$  is given by  $S(A) = -\text{Tr}_A \rho_A \ln \rho_A$ , where  $\rho_A$  is the reduced density matrix of  $A$  obtained by tracing out degrees of freedom in the complement  $A^c$ :  $\rho_A = \text{Tr}_{A^c} \rho$ . In this work, we consider pure states  $\rho = |\psi\rangle\langle\psi|$ . The EE for a spatial bipartition of a quantum Hall state described by a trial wave function at filling  $\nu$ , an example being the electronic Laughlin state at  $\nu = \frac{1}{3}$ , should take the general form

$$S(A) = c \frac{L_A}{\ell_B} - \gamma_{\text{top}} - \gamma_{\text{geo}} + \dots, \quad (1)$$

where  $L_A$  is the perimeter of subregion  $A$ , which we take to be much larger than the magnetic length  $L_A \gg \ell_B$ , and the ellipsis denotes terms that vanish at large  $L_A/\ell_B$ . The first term is the area (or boundary) law that is generally present for the low-energy states of local Hamiltonians without a finite Fermi surface. Here, the magnetic length  $\ell_B$  plays the role of the microscopic (UV) length scale. In contrast, in a lattice model this role would be played by the lattice spacing, whereas a UV cutoff would appear in a continuum quantum field theory. Let us now examine the subleading corrections parametrized by  $\gamma$ , as these contain more useful

<sup>1</sup>This is true at sufficiently low temperatures.

information about the state. First,  $\gamma_{\text{top}} \geq 0$  is the universal topological contribution arising from the topological order associated with the gapped phase [1–5]. It detects the presence of anyon excitations, and is thus absent at integer filling for fermions. As its name suggests,  $\gamma_{\text{top}}$  does not depend on the geometry of subregion  $A$ . This term has been widely studied, and can be obtained using topological quantum field theory (TQFT). For example, for Laughlin states at fractional filling  $\nu = 1/m$ , with  $m$  odd, it is  $\gamma_{\text{top}} = \frac{1}{2} \ln m$  [1]. The next term,  $\gamma_{\text{geo}}$ , is a geometric contribution. For Laughlin states, it is “universal” in the sense that, just as  $\gamma_{\text{top}}$ , it does not depend on  $\ell_B$  or any other scale. It is a pure number that only depends on the shape of subregion  $A$  and the state under consideration.

An important class of shapes has corners or cusps, such as a triangle or a square. The EE of such nonsmooth subregions has been extensively studied in the ground states of gapless Hamiltonians, such as conformal field theories [8,11–14,18–24]. It was found that the subleading correction  $\gamma$  contains a contribution diverging logarithmically with the perimeter  $\sum_i a(\theta_i) \ln(L_A/\epsilon)$ , where  $\epsilon$  is a short-distance cutoff. The prefactor  $\sum_i a(\theta_i)$  depends on the geometry of  $A$  through the angles of its corners  $\theta_i$ . In a variety of states, it was shown that the *corner function*  $a(\theta)$  captures key information about long-distance physics of the quantum critical state, and shows surprising universality. As a concrete example, when the corner is nearly smooth  $\theta \approx \pi$ , the corner function yields the stress tensor central charge  $C_T$  of conformal field theories in two spatial dimensions [13,14,22]. This central charge controls the two-point function of the stress tensor (thus of the energy density), as well as the finite-frequency shear viscosity.

In ground states of gapped systems, like quantum Hall states, the logarithmic divergence is cut off by the finite correlation length. In that case, we expect that a polygon-shaped region will yield the following subleading term, with  $i$  again labeling the corners:

$$\gamma_{\text{geo}} = \sum_i a(\theta_i) \quad (2)$$

that does not diverge with the size of region  $A$ , in contrast to critical states. For trial wave functions such as the Laughlin states, the corresponding corner function  $a(\theta)$  is a pure number independent of all scales. For the quantum critical states described above, this pure number is multiplied by a logarithm  $a(\theta) \ln(L_A/\epsilon)$ , which preserves the cutoff ( $\epsilon$ ) independence of  $a(\theta)$ . The function  $a(\theta)$  has been computed numerically for the integer quantum Hall state at  $\nu = 1$  [25]. However, the physical information encoded by this function remains unknown, even in the simplest case at  $\nu = 1$ . It has yet to be computed at fractional fillings.

In this work, we revisit the calculation of  $a(\theta)$  at  $\nu = 1$  using analytical insights as well as high-precision numerics. We also study the entire reduced density matrix  $\rho_A$  through its Schmidt spectrum and eigenstates. We further extend our calculations to the ground state at filling  $\nu = 2$ , as well as to the excited state at  $\nu = 1$  obtained by filling the first Landau level and leaving the lowest Landau level (LLL) unoccupied. When only the first LL is occupied (zeroth level empty), we find surprising relations to the results for the ground state at  $\nu = 1$ , helping shed light on the physics encoded in the corner

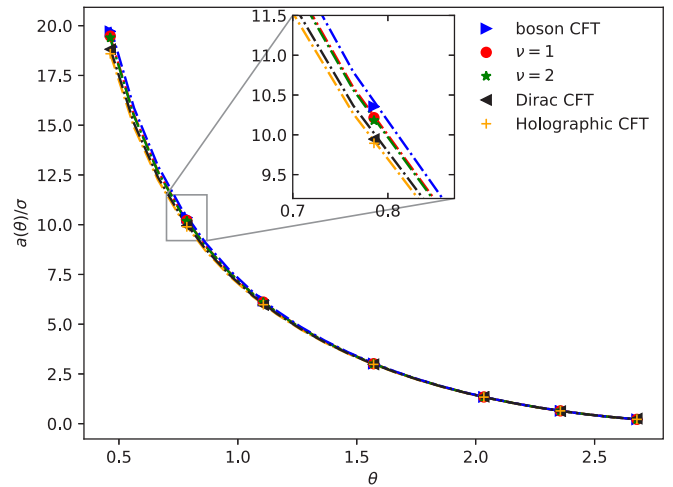


FIG. 1. Comparison of corner functions (as functions of the corner angle  $\theta$ ) for various systems in two spatial dimensions, normalized by the smooth-limit coefficient  $\sigma$ . The integer quantum Hall ground states at fillings  $\nu = 1, 2$  are computed in this work. The boson conformal field theory (CFT) corresponds to noninteracting massless relativistic bosons [16], which have the same corner function as the large- $N$   $O(N)$  Wilson-Fisher fixed point [23]. The Dirac CFT is a theory of massless Dirac fermions [16], while the holographic CFT corresponds to a strongly interacting supersymmetric CFT described by the AdS/CFT correspondence. Data markers correspond to lattice simulations (except for the holographic CFT [20]), while continuous lines correspond to the ansatz (10), except for the boson and Dirac CFT where a more precise ansatz is used [16].

function. We push the comparison further by comparing the corner function to the one obtained for various conformal field theories in two spatial dimensions, including gapless Dirac fermions. We find that the Hall corner function, when properly normalized, has a surprisingly close shape dependence to the conformal theories, as shown in Fig. 1. We also examine the role of anisotropy on the EE, and show that it strongly affects its shape dependence. Going beyond the EE, we analyze the low-lying entanglement spectrum and the corresponding eigenfunctions, which reveal “excitations” localized near corners. Finally, we study a different type of corner where two tips touch at a point (“hourglass”), and we extract a universal quantity via the mutual information.

The rest of the paper is organized as follows: Section II describes how to obtain the reduced density matrix, entanglement spectrum, and EE for IQH states. Section III contains the results for these quantities for simple regions that contain a corner. Section IV describes the effects of mass anisotropy on the EE. Section V studies a new type of region where two corners touch at a point. This geometry can be used to define a quantum mutual information that is independent on the microscopic information of the IQH states. Finally, in Sec. VI we summarize our main findings and present an outlook for interacting systems, including fractional quantum Hall states. Appendices A and B provide detailed information regarding our numerical results.

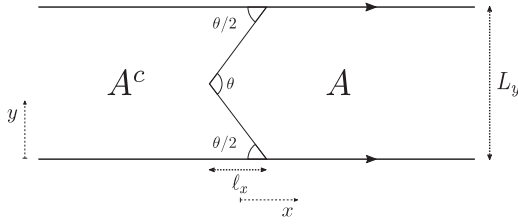


FIG. 2. The “arrow-shaped” subregion  $A$  and its complement in an infinite cylinder of circumference  $L_y$ .  $A$  has two corners of angles  $\theta$  and  $2\pi - \theta$ . The arrows on the top and bottom of the drawn rectangle indicate the equivalent points.

## II. ENTANGLEMENT IN INTEGER QUANTUM HALL STATES

The IQH system can be described by considering the following single-electron Hamiltonian in the Landau gauge:

$$H = \frac{p_x^2}{2m_e} + \frac{(p_y + eBx)^2}{2m_e}, \quad (3)$$

where  $m_e$  is the effective mass of the electrons. On a cylinder of circumference  $L_y$  (shown in Fig. 2), the eigenstates of  $H$  are the usual Landau level (LL) wave functions of energy  $E_n = \hbar\omega_c(n + \frac{1}{2})$ :

$$\phi_{n,k}(x, y) = d_n e^{iky} H_n(x + k\ell_B^2) \exp\left(-\frac{(x + k\ell_B^2)^2}{2\ell_B^2}\right), \quad (4)$$

$$n = 0, 1, 2, \dots$$

The  $y$  periodicity leads to discrete wave vectors  $k = 2\pi m/L_y$  with  $m \in \mathbb{Z}$ . The key scale of the problem is the magnetic length  $\ell_B = \sqrt{\hbar/eB}$ , and the cyclotron frequency  $\omega_c = eB/m_e$  gives the gap between LLs.  $H_n$  are Hermite polynomials, and the normalization coefficient is  $d_n = \pi^{-1/4}/\sqrt{2^n n! \ell_B L_y}$ . For IQH states, the system’s wave function is obtained by entirely filling one or more LLs with electrons of every  $y$  momentum  $k$ . We will consider the ground states at  $\nu = 1$  and  $2$ . We will also study a special excited eigenstate at  $\nu = 1$  where every electron is in the  $n = 1$  LL, which we will call the first LL excited state. In our analysis, we shall set  $\ell_B = 1$ .

We want to study the reduced density matrix of these states for various subregions  $A$  of the cylinder. In particular, we will examine the entanglement spectrum, EE, and eigenstates of the reduced density matrix  $\rho_A$ . Since we deal with noninteracting electrons, we can use the method developed in [26]. The eigenvalues of  $\rho_A$  can be computed from the eigenvalues of the correlation function  $C_{\mathbf{r},\mathbf{r}'} = \langle c_{\mathbf{r}}^\dagger c_{\mathbf{r}'} \rangle$  restricted to subregion  $A$ , where averages are computed in the state of the total system  $A \cup A^c$ . For our IQH states, it is possible to discretize this eigenvalue problem, as shown in [25], by diagonalizing a block matrix given by

$$\mathcal{F}_{k,k'}^{(n,n')}(A) = \int_A d^2\mathbf{r} \phi_{n,k}(\mathbf{r}) \phi_{n',k'}^*(\mathbf{r}), \quad (5)$$

where for each pair of momenta  $\{k, k'\}$  one has a block corresponding to the occupied LLs. In the simplest case of the IQH at  $\nu = 1$ , the block is only a number. For the IQH at  $\nu = 2$  we have a  $2 \times 2$  block corresponding to  $n = 0, 1$ ; the

$(0,1)$  and  $(1,0)$  off-diagonal elements measure the overlap in  $A$  between electrons in the LLL and the first LL. For numerical computations to be possible, one needs to truncate the infinite-dimensional  $\mathcal{F}$  matrix. The natural way to do so is to work with matrices with  $\{k, k'\}$  smaller than a certain cutoff. This amounts to considering only states  $\phi_{n,k}$  centered not too far from the cut. Increasing the cutoff should then lead to convergent results since far away electrons contribute negligibly to the entanglement between  $A$  and  $A^c$ .

From the discussion above, we understand that the spectrum of the correlator  $C$  is of great importance. It is actually directly related to the entanglement spectrum (ES) which is defined as the spectrum of  $-\ln \rho_A$  (up to a shift of the zero of the spectrum). Indeed, we can first relate the ES to the *single-particle* spectrum of the entanglement Hamiltonian  $H_A$  defined as  $\rho_A = \frac{1}{Z} \exp(-H_A)$  [27], which in the case of free fermions is a free-fermion quadratic Hamiltonian restricted to subregion  $A$ :  $H_A = \sum_{\mathbf{r},\mathbf{r}' \in A} h_{\mathbf{r},\mathbf{r}'} c_{\mathbf{r}}^\dagger c_{\mathbf{r}'}$ . The eigenvalues  $\epsilon$  of  $h$  (which we refer to as the spectrum of  $H_A$ ) can be obtained from the eigenvalues of the correlation matrix by the relation  $h^T = \ln(\frac{1-C}{C})$  [26]. In this work, we numerically compute the eigenvalues  $\lambda$  of the correlation matrix  $C$ . The relation between the two spectra is then given by the matrix relation given just above or, equivalently, by  $\lambda = \frac{1}{1+\epsilon^\epsilon} = n_F(\epsilon)$ , where  $n_F$  is the Fermi-Dirac distribution. We will from now on refer to the single-particle spectrum of  $H_A$  as the ES since one can reconstruct the full spectrum of  $\rho_A$  from the eigenvalues of  $h$ .

## III. CORNER ENTANGLEMENT

We are interested in computing the ES and various EEs for IQH states (in which  $\gamma_{\text{top}}$  vanishes), for domains  $A$  with nonsmooth boundaries, and with a perimeter that far exceeds the magnetic length  $L_A/\ell_B \gg 1$ . In contrast, for smooth regions (where smoothness is defined relative to the scale  $\ell_B$ ) the residual part of the EE  $\gamma_{\text{geo}}$  vanishes [28,29], as can be seen for a flat cut on the cylinder (see below). This makes the corner geometry even more important for the states under consideration. We will calculate the corner contributions to the EE and ES of the arrow-shaped subregion of an infinite cylinder of circumference  $L_y$  presented in Fig. 2, where the smooth cut is obtained by setting  $\theta = \pi$ . Note that due to the periodicity in the  $y$  direction,  $A$  contains two corners of angles  $\theta$  and  $2\pi - \theta$ .

### A. Entanglement spectrum

As can be seen in Fig. 3, the presence of corners results in a deformation of the ES compared to that of a smooth cut for the  $\nu = 1$  and filled first LL states. In the case of a smooth cut, an analytical formula exists for the ES of the  $\nu = 1$  state [28], and, in general, for all ES of filled  $n$ th LL states. For a smooth cut in the  $y$  direction, the spectrum can be expressed as a function of the  $y$  momentum  $k$ . At small  $k$ , we can easily show that an even  $n$  (including  $n = 0$ ) results in a linear dispersion  $\epsilon(k) \propto k$ , whereas, for an odd  $n$ , we have  $\epsilon(k) \propto k^3$ . A sublinear dispersion was also previously observed in the first LL excited state for smooth subregions (using a spherical geometry instead of the cylinder) [30]. For the simplest case of the  $\nu = 1$  IQH ground state ( $n = 0$ ),

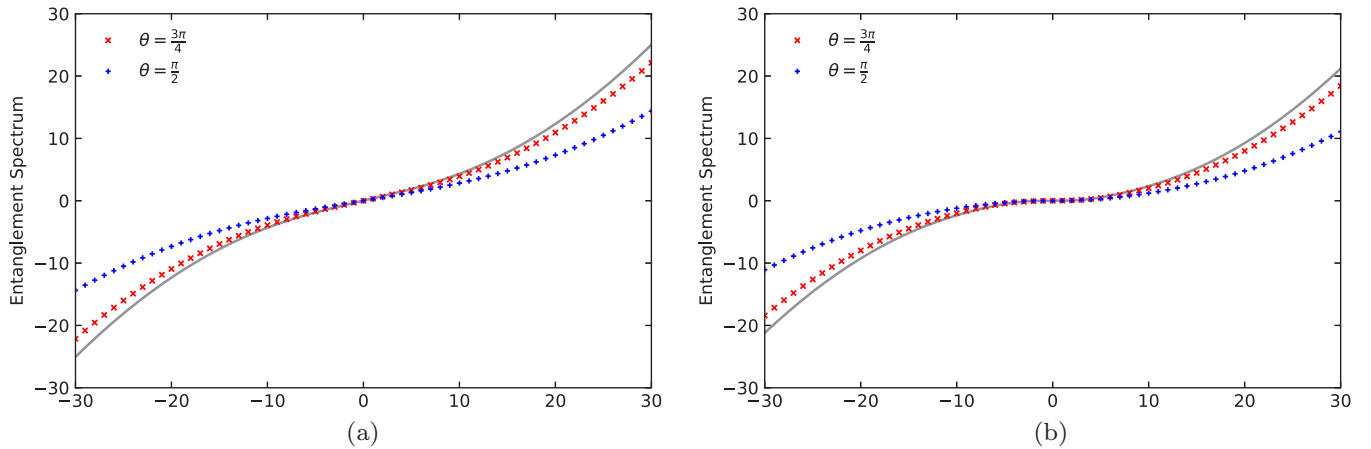


FIG. 3. Entanglement spectra. The continuous lines are the spectra associated to a smooth cut, while the discrete points correspond to arrow-shaped domains of corner angle  $\theta$ . Each spectrum associated to a nonsmooth cut is presented in increasing order, with integer spacing, with the zero pseudoenergy point centered at the origin. In order to compare the smooth and nonsmooth results, the spectra associated to the smooth cut are presented not as functions of  $y$  momentum  $k$ , but of  $\frac{kL_y}{2\pi}$ .

the linear dispersion matches the dispersion of a chiral mode on a physical edge, in agreement with the connection between entanglement cuts and physical edges [4]. For the first LL excited state (all fermions have  $n = 1$  wave functions), the dispersion is cubic at small  $k$ , and thus does not have the expected dispersion for the corresponding physical edge mode.

For the  $\nu = 2$  state, it is harder to determine the influence of corners directly on the entanglement spectrum. The reason is that in the smooth case, there are actually two eigenvalues for each  $k$ , as shown in Fig. 4(a). A similar spectrum was obtained on the sphere [30]. After computing the eigenvalues numerically for the case of the “arrow-shaped” domain with  $\theta = \pi/2$ , we obtain couples of roughly the same value at low pseudoenergy, which we guess would belong to deformations of the two distinct smooth spectra. The degeneracy is broken as the pseudoenergies move away from zero. This situation is shown in Fig. 4(b).

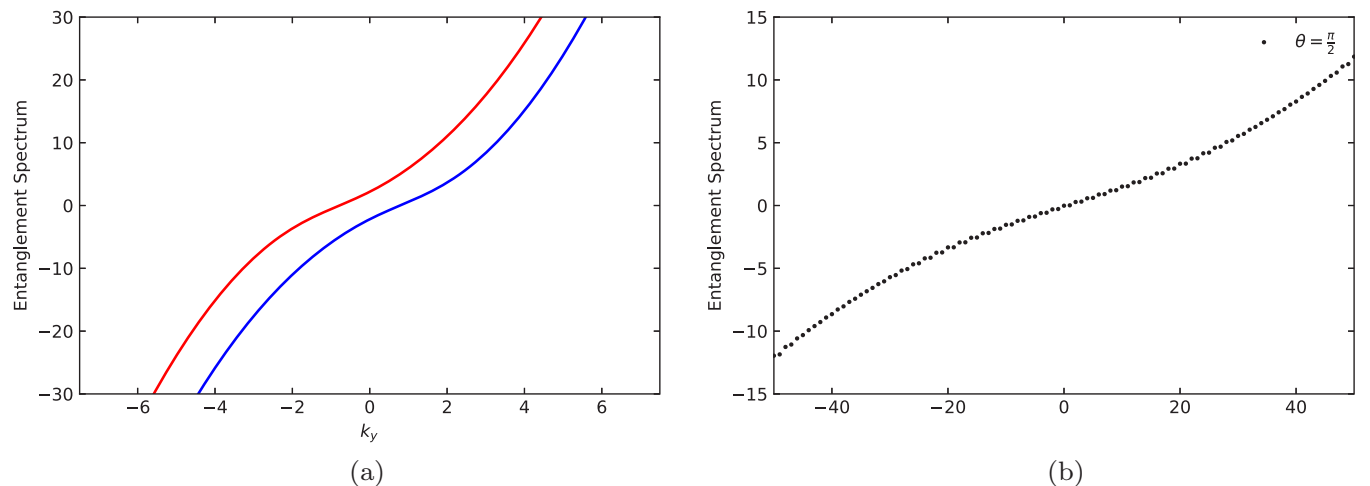


FIG. 4. Entanglement spectra in the  $\nu = 2$  ground state. Again, the spectrum associated to the nonsmooth cut is presented in increasing order with integer spacing.

## B. Entanglement excitations

In addition to the eigenvalues of the correlator  $C_{r,r}$ , one can study its eigenfunctions. Let us focus on the  $\nu = 1$  ground state for brevity. One can reconstruct a (continuous) eigenfunction of  $C$ , for an eigenvalue  $\lambda$ , from the associated discrete eigenvector of the  $\mathcal{F}$  matrix as follows [25]:  $\psi(x, y) = \sum_k \phi_{0,k}^*(x, y) A_k$ , with  $A_k$  the components of the normalized eigenvector associated with the eigenvalue  $\lambda$ . We find that the eigenfunctions associated with the low-lying part of the eigenspectrum  $\epsilon$  localize close to the entanglement cut, as shown in Fig. 5. They decay exponentially fast at beyond a few magnetic lengths of the cut, as expected. We observe that the zero pseudoenergy eigenfunction has equal maxima at both corners, as shown in Figs. 5(c) and 5(d). The further the pseudoenergies  $\epsilon$  are from zero, the further the eigenfunctions are located from the cut. We observe a gradual disappearance of one or the other maximum when transitioning from  $\epsilon = 0$  to  $|\epsilon| > 0$ . For the computations, we used  $L_y = 25$  and  $\theta = \frac{\pi}{2}$ .

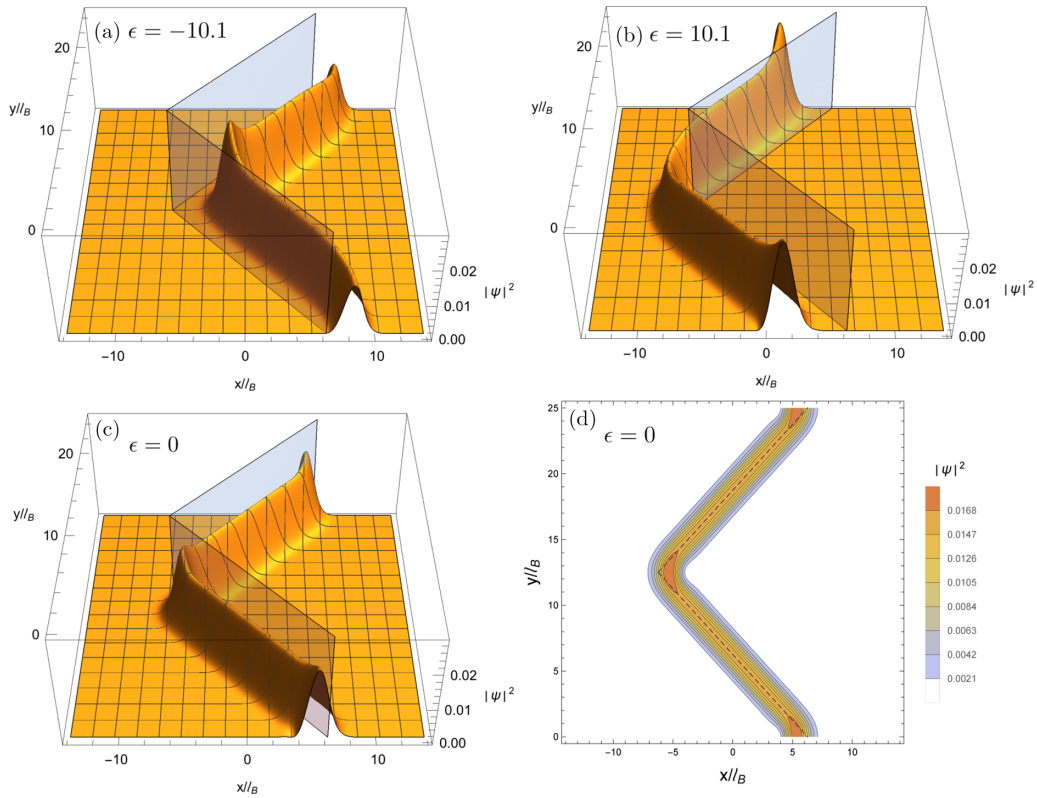


FIG. 5. Eigenfunctions of the correlator  $C$ . The light gray region (dotted line for the contour plot) in each panel represents the entanglement cut between  $A$  and  $A^c$ . The  $\epsilon = 0$  eigenfunction has zero pseudoenergy to machine precision.

Even though the eigenfunctions of  $C$  are defined only on  $A$ , we have decided to show their extensions to the whole space  $A \cup A^c$ . Not surprisingly, if we had chosen the left side of the cut as  $A$ , we would have found that the new eigenfunctions of energy  $\epsilon$  would be our old eigenfunction with energy  $-\epsilon$ .

We mention that similar behavior was observed for the eigenfunctions obtained in a geometry where the corner is adjacent to a physical boundary [31].

### C. von Neumann entanglement entropy

We can compute the von Neumann EE with the relation

$$S(A) = \sum_{\lambda} [-\lambda \ln(\lambda) - (1 - \lambda) \ln(1 - \lambda)]. \quad (6)$$

For pure states, since  $S(A) = S(A^c)$ , the corner function has reflection symmetry about  $\theta = \pi$ :  $a(\theta) = a(2\pi - \theta)$ . The two corners of our arrow-shaped region thus contribute  $a(\theta) + a(2\pi - \theta) = 2a(\theta)$ . Also, the smooth limit gives  $a(\pi) = 0$  by definition since the corner is absent in this limit. We can use this fact to determine the proportionality constant  $c$  of the area law in Eq. (1) [28]. The corner function for the von Neumann EE is then obtained for our arrow-shaped domain  $A$  by subtracting the area law:

$$a(\theta) = -\frac{1}{2}[S(A) - cL_A], \quad (7)$$

where the perimeter of  $A$  is  $L_A = 2\sqrt{\ell_x^2 + (L_y/2)^2}$ . Equation (7) holds in the limit  $L_A \gg 1$  so that terms of  $O(1/L_A)$  are negligible. The required size of  $L_A$  is discussed in Appendix B.

We show the high-precision numerical results for the corner function in Fig. 6 for the  $\nu = 1, 2$  ground states and for the filled first LL excited state. A subset of the  $\nu = 1$  data was previously obtained (to a lower precision) in [25]. Some of the numerical data used to produce this figure are presented in Table II of Appendix A.

First, we observe that the three curves show the same small and large angle behavior, which we will discuss in more detail below. In addition, one may naively expect that the  $\nu = 2$  ground state would have a corner function that is the double

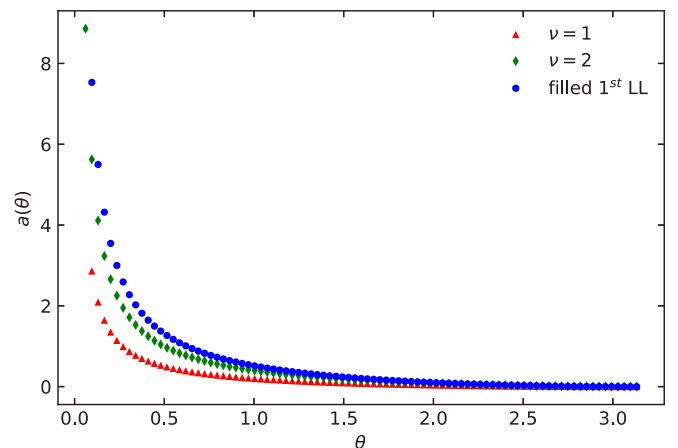


FIG. 6. Corner functions for our three IQH states as a function of the opening angle  $\theta$ . Each curve behaves as  $1/\theta$  at small angles, and  $(\theta - \pi)^2$  in the smooth limit.

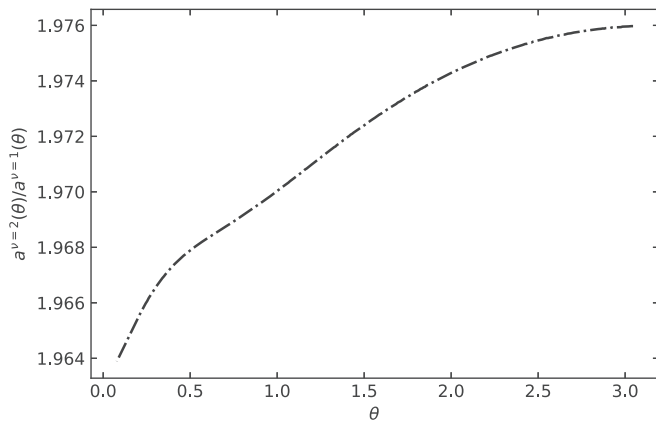


FIG. 7. Ratio of corner functions for the ground states at  $\nu = 1, 2$ . It nearly equals the naively expected value 2, but is clearly below it.

of the one at  $\nu = 1$ . However, the situation is not as simple since the  $n = 0$  and 1 wave functions are not only distinct, but also they are not orthogonal on subregion  $A$ , which leads to off-diagonal elements in the correlation matrix  $\mathcal{F}$ , Eq. (5). Surprisingly, Fig. 7 shows that the ratio of the  $\nu = 1, 2$  corner functions is almost constant and equal to 2, but is nevertheless clearly below this naive value. In Fig. 6, we also see that the first LL excited state has the largest corner function, even exceeding the one at  $\nu = 2$ . This is again due to the fact that the contributions from different LLs are not additive.

In the limit of small angles, we observe the scaling

$$a(\theta) = \frac{\kappa}{\theta} + \dots \quad (8)$$

for all three states considered. This small-angle divergence is also observed in CFTs [8,20]. For the  $\nu = 1$  state, we numerically obtain  $\kappa \approx 0.276$  by analyzing the behavior of  $\theta a(\theta)$  for sufficiently small angles ( $\theta \approx 0.05$ ). The  $\kappa$  coefficients for the three states are given in Table I.

In the nearly smooth limit, we have

$$a(\theta) = \sigma(\theta - \pi)^2 + \tilde{\sigma}(\theta - \pi)^4 + O[(\theta - \pi)^6] \quad (9)$$

owing to the nonsingular nature of the  $\theta \rightarrow \pi$  limit, which is in contrast to the pole obtained as  $\theta \rightarrow 0$  [Eq. (8)]. Only even powers appear due to the reflection symmetry mentioned above,  $a(\theta) = a(2\pi - \theta)$ . For the  $\nu = 1$  state, we obtain  $\sigma \approx 0.02836$  and  $\tilde{\sigma} \approx 0.0019$ . The values of  $\sigma$  for the two other states under study are given in Table I. Those results were obtained by fitting numerical values of  $\frac{a(\theta)}{(\theta - \pi)^2}$  for angles near  $\pi$  ( $\theta \approx 3.05$ ) to the expected quadratic behavior.

TABLE I. Coefficients for the asymptotic behavior of  $a_\alpha(\theta)$  for Rényi indices  $\alpha = 1, 2$ . Numerical values presented for  $\sigma_\alpha$  are rounded, and were stable up to their last digit. The same goes for values presented in Table II of Appendix A, and in the end of Sec. IV. The error on numerical values of all  $\kappa_\alpha$  is estimated at  $\pm 0.001$ .

	$\alpha = 1$			$\alpha = 2$		
	$\nu = 1$	Filled first LL	$\nu = 2$	$\nu = 1$	Filled first LL	$\nu = 2$
$\sigma_\alpha$	0.02836	0.06895	0.05603	0.02064	0.07614	0.04152
$\kappa_\alpha$	0.276	0.727	0.542	0.192	0.627	0.387

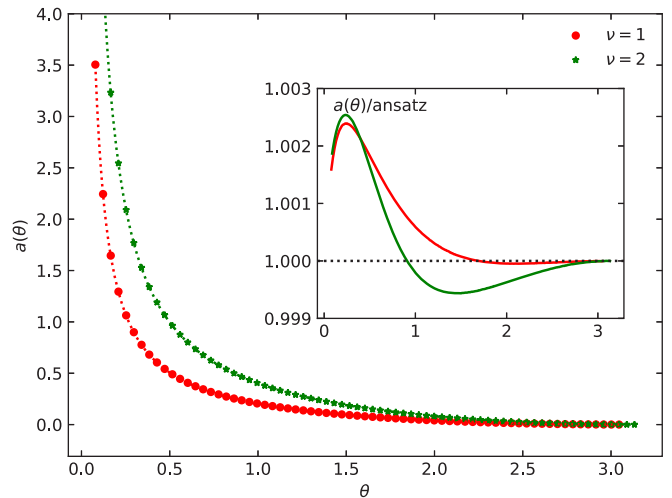


FIG. 8. Comparison between numerical values of the corner function for the  $\nu = 1$  and 2 ground states to the ansatz made in [13]. We see that the agreement between the numerical points and the ansatz, represented by the dotted lines, is excellent. The inset shows the ratio between the numerical corner function (interpolated) and the ansatz.

It is interesting to note that a simple ansatz proposed in [13] gives an approximate analytical formula for the corner function, which is exact at both asymptotic limits:

$$a(\theta) \simeq \mu_1 \frac{(\pi - \theta)^2}{\theta(2\pi - \theta)} - \mu_2 [1 + (\pi - \theta) \cot \theta], \quad (10)$$

where  $\mu_1 = 2\pi \frac{\kappa - 3\pi\sigma}{\pi^2 - 6}$  and  $\mu_2 = \frac{3}{\pi} \frac{2\kappa - \pi^3\sigma}{\pi^2 - 6}$  are determined by the inputted smooth and sharp limit coefficients. It is interesting to note that the function multiplied by  $\mu_2$  appears in the result for the particle variance for a pie-shaped region of opening angle  $\theta$  not only for the integer quantum Hall ground state at  $\nu = 1$  [32], but also for a very large class of classical and quantum states [33]. We note in passing that this ansatz also works for the Rényi entropies, which will be studied in the next subsection. From Fig. 8, we see that Eq. (10) works very well for both fillings. By construction, the ratio between the ansatz and the numerical data approaches unity at small and large angles.

The leading constant  $\sigma$  in Eq. (9) is particularly important as we can use it to define a normalized corner function:  $a(\theta)/\sigma$ . The normalized corner functions for the  $\nu = 1, 2$  ground states are shown in Fig. 1, where they are compared to a variety of ground states of gapless two-dimensional systems described by CFTs. We note that for CFTs, the corner function

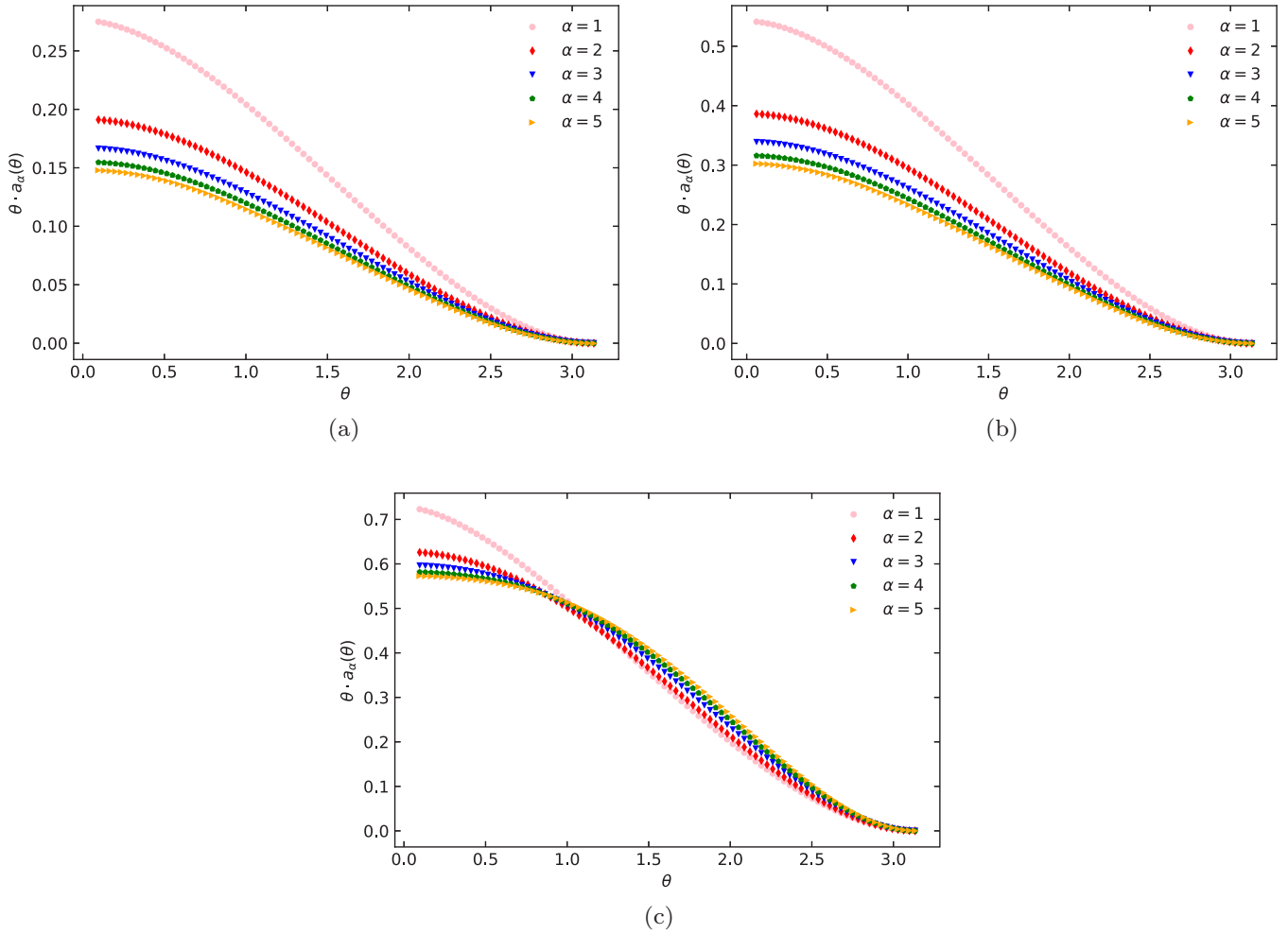


FIG. 9.  $\theta a_\alpha(\theta)$  as a function of corner angle  $\theta$  for the first five integer Rényi indices.

$a(\theta)$  comes multiplied by a logarithm  $\ln(L_A/l_{UV})$  owing to gapless nature of the state. This logarithm does not spoil the universality of  $a(\theta)$  but only of the constant subleading term. We observe that the normalized corner functions for these Hall states are in fact bounded below by the one for the massless Dirac fermion CFT, and upper bounded by the massless boson CFT. In particular, this means that the Hall functions exceed the lower bound that holds for all CFTs [18],

$$a(\theta)/\sigma \geq 8 \ln[1/\sin(\theta/2)] \tag{11}$$

although the Hall Hamiltonian has *a priori* nothing to do with a CFT in two spatial dimensions. A stronger bound was conjectured to hold for CFTs in [34]:  $a(\theta)/\sigma$  is minimal for a strongly coupled supersymmetric CFT that is holographically dual, via the AdS/CFT correspondence of string theory, to Einstein gravity in one higher dimension. In Fig. 1, it can indeed be seen that the  $\nu = 1, 2$  curves are above the holographic one. These findings suggest that the conjectured bound of [34] could extend to a much broader class of quantum systems. In particular, the bound holds for the first LL excited state (not shown in Fig. 1) since  $a(\theta)/\sigma$  for that state exceeds the normalized corner functions of both the  $\nu = 1, 2$  ground states.

For the Hall states under study, it would be of interest to determine the physical meaning of  $\sigma$ . For CFTs,  $\sigma$  has in fact

a very simple interpretation [14,34]:  $\sigma = \pi^2 C_T/24$ , where  $C_T$  is the stress-tensor “central charge.” In other words,  $C_T$  determines the two-point function of the stress tensor (a local operator) in the ground state of the CFT, which includes the autocorrelations of the energy density. It would be interesting to see whether  $\sigma$  for the Hall systems also possesses an interpretation in terms of local observables.

#### D. Rényi entropies

We now study the Rényi EE  $S_\alpha(A)$  of our IQH states, where  $\alpha$  is the Rényi index.  $S_\alpha(A)$  obeys the following large perimeter expansion:

$$S_\alpha(A) = c_\alpha \frac{L_A}{\ell_B} - \sum_i a_\alpha(\theta_i) + O(\ell_B/L_A), \tag{12}$$

where we have temporarily reinstated  $\ell_B$ . We can then extract the corner functions by the same method as above except now EEs are connected to ESs by  $S_\alpha(A) = \frac{1}{1-\alpha} \sum_\lambda \ln[\lambda^\alpha + (1-\lambda)^\alpha]$ . Figure 9 presents the corner functions for the first few integer Rényi indices, for each of our IQH states.

One property of the Rényi EE is that it is decreasing as a function of  $\alpha$ . We indeed numerically verified this to be true

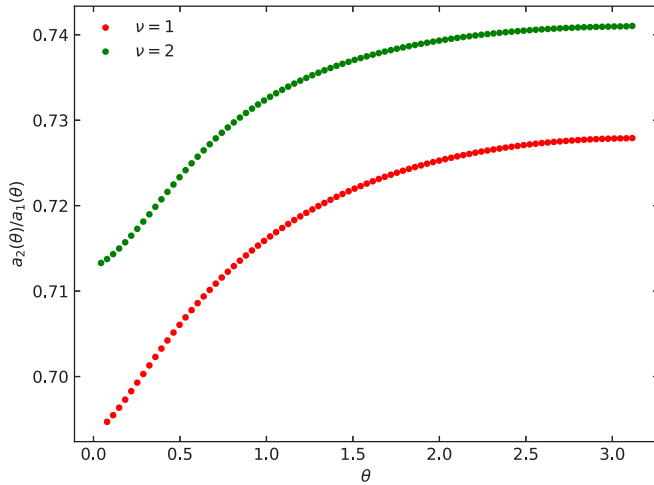


FIG. 10. Comparison of Rényi EE for indices  $\alpha = 1, 2$  for the two ground states at fillings  $\nu = 1, 2$ .

when considering our “arrow-shaped” domain with two corners for multiple angles, regardless of the fact that the corner function is *decreasing* as a function of  $\alpha$  for the  $\nu = 1$  and 2 states, or that it exhibits a more complicated behavior for the filled first LL state. In fact, the decrease in the proportionality constant of the boundary law that is the dominant term in the studied regime where  $L_A \gg 1$ . It is worth noting that the nonmonotonously decreasing behavior of the corner function of the excited first LL state is clearly distinct from what is obtained for the ground states at  $\nu = 1, 2$ , as well as for the massless bosons and Dirac fermion CFTs [16].

The same small- and large-angle behavior as described in Sec. III C is observed for the Rényi corner functions  $a_\alpha(\theta)$ . The various coefficients for the asymptotic behavior are, in this case, denoted by  $\kappa_\alpha$  and  $\sigma_\alpha$ , and their numerical values are presented in Table I for  $\alpha = 2$ .

We find that for the IQH states, the EEs of different Rényi indices do not factorize, i.e., cannot be written as  $a_\alpha(\theta) = f(\alpha)a_1(\theta)$ . Indeed, if this were the case, the ratio  $a_2(\theta)/a_1(\theta) = f(2)$  would be a constant for all  $\theta$ , which, as shown in Fig. 10, is not the case for  $\nu = 1$  and 2 states. Interestingly, the observed values for the ratio  $a_2/a_1$  are relatively close to what one would obtain if the Rényi index dependence factorized with  $f(\alpha) = (1 + \alpha^{-1})/2$ , which is reminiscent of one-dimensional CFTs [35].

#### IV. ANISOTROPIC STATES

In this section, we will study the effects of anisotropy on the EE. Specifically, we will break the rotational symmetry of the quantum Hall system by choosing different masses along the  $x$  and  $y$  directions, which results in the following single-particle Hamiltonian:

$$H = \frac{p_x^2}{2m_x} + \frac{(p_y + eBx)^2}{2m_y}. \quad (13)$$

Such mass anisotropy is relevant for the description of 2DEGs with anisotropic band masses (such as AlAs or Si), uniaxial stress, or a tilted magnetic field. A more detailed discussion about this can be found in Ref. [36]. The anisotropic single-

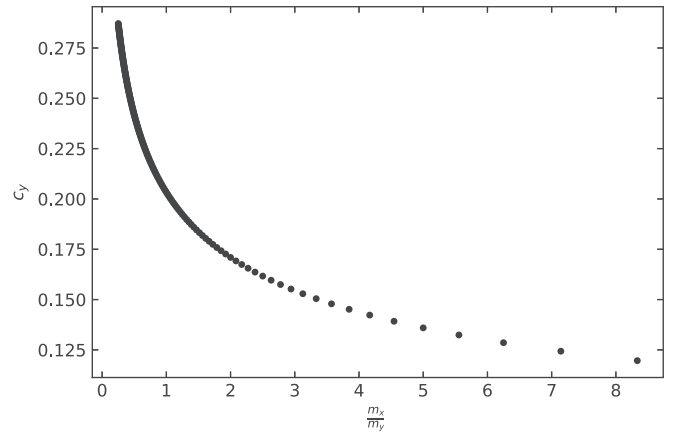


FIG. 11. Boundary-law coefficient for a smooth cut in the  $y$  direction of the anisotropic quantum Hall state at filling  $\nu = 1$  as a function of mass ratio  $m_x/m_y$ .

electron wave function in the LLL becomes

$$\phi_{0,k} = \frac{1}{\pi^{1/4} \sqrt{\ell_B L_y}} \left( \frac{m_x}{m_y} \right)^{\frac{1}{8}} e^{iky} \exp \left( -\sqrt{\frac{m_x}{m_y}} \frac{(x + k\ell_B^2)^2}{2\ell_B^2} \right). \quad (14)$$

In the presence of anisotropy, the LL energy spectrum becomes  $E_n = \hbar \tilde{\omega}_c (n + \frac{1}{2})$ , with the modified cyclotron frequency  $\tilde{\omega}_c = \frac{eB}{\sqrt{m_x m_y}}$ . For a smooth cut in the  $y$  direction, we verify the boundary law of the von Neumann EE and obtain the proportionality constant  $c_y$  ( $y$  to indicate a smooth cut along the  $y$  direction) for different mass ratios  $m_x/m_y$ . As shown in Fig. 11,  $c_y$  approaches 0 as the mass ratio  $m_x/m_y$  tends to infinity, which is a consequence of the fact that electrons become more localized along the  $x$  direction [see Eq. (14)]. The opposite phenomenon occurs at small mass ratio.

For our arrow-head geometry, the breaking of rotational symmetry modifies the boundary law as follows:

$$2c\sqrt{\ell_x^2 + (L_y/2)^2} \rightarrow 2\sqrt{(c_x \ell_x)^2 + (c_y L_y/2)^2}, \quad (15)$$

where  $c_x$  is the boundary-law constant that would be obtained for a flat cut parallel to the  $x$  axis. By symmetry,  $c_x$  at a given mass ratio is given by  $c_y$  with the ratio inverted  $c_x(m_x/m_y) = c_y(m_y/m_x)$ . We note that  $c_x = c_y$  only if the masses are equal. The corner contributions also inherit such a dependence on orientation. In the presence of mass anisotropy, we denote the corner function  $a(\theta, \hat{\mathbf{u}})$ , where  $\hat{\mathbf{u}}$  is the unit vector parallel to the bisector of the corner  $\theta$  pointing inwards of subregion  $A$ . By assuming that the contribution of a corner is unchanged by a reflection of this corner along the  $x$  and/or  $y$  axis, which seems reasonable considering the symmetries of the system, we should still be able to extract the contribution of a corner with bisector oriented along the  $x$  axis  $a(\theta, \hat{\mathbf{x}})$  from the same arrow-shaped region of Fig. 2 used until now. We can then study the dependence on the mass ratio  $m_x/m_y$  of a corner of this particular orientation, which is what is presented in Fig. 12(a) for the  $\nu = 1$  state. From Fig. 12(b), we see that the corner function for a given opening angle grows with the mass ratio  $m_x/m_y$ . This growth leads to a *decrease* of the total



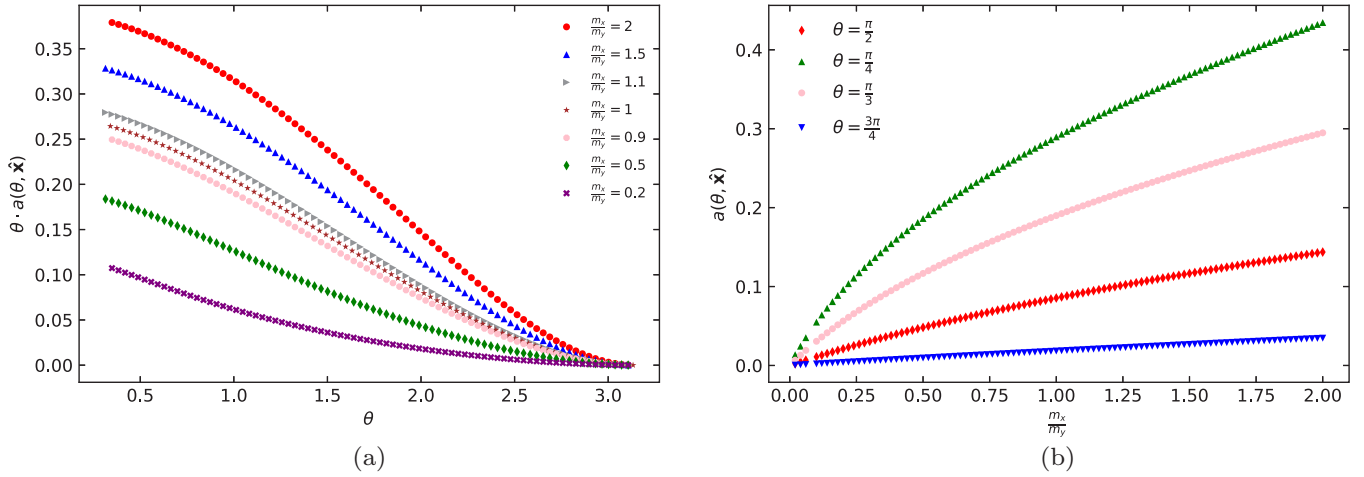


FIG. 12. Mass ratio  $m_x/m_y$  effect on the corner function, for corner with bisector along the  $x$  axis, in the anisotropic quantum Hall state of filling  $\nu = 1$  for the arrow-shaped domain.

EE since the corner contribution appears with a negative sign  $-\sum_i a(\theta_i, \hat{u}_i)$ .

Finally, we observe a peculiar behavior of the orientation dependence of the corner function. By computing the EE for a simple square with edges parallel to the  $x$  and  $y$  axes (see Fig. 13), we observe *no* dependence of the corner function on the mass ratio, so that the corner function (tested for mass ratios  $m_x/m_y \in \{2, 5, 50\}$ ) corresponds to that for a unit mass ratio to at least eight significant digits:  $a(\frac{\pi}{2}, \frac{1}{\sqrt{2}}(\hat{x} + \hat{y})) = 0.085498696$ . We also find by considering a rotated square with angle bisectors oriented along the  $x$  and  $y$  axes (see Fig. 13), that the corner contribution  $a(\frac{\pi}{2}, \hat{y})$  is that of a corner whose bisector is oriented along the  $x$  axis  $a(\frac{\pi}{2}, \hat{x})$  but with an inverted mass ratio, consistent with the  $\pi/4$  rotational symmetry. For example, we can extract from a calculation with the arrow-shaped domain that the contribution of a corner whose bisector is oriented along the  $x$  axis that for a mass ratio  $m_x/m_y = \frac{1}{2}$ ,  $a(\frac{\pi}{2}, \hat{x}) = 0.0481848$ . This way, when considering our tilted square, we should have  $a(\frac{\pi}{2}, \hat{y}) = -\frac{1}{2}(S - 2 \cos \frac{\pi}{4} \sqrt{c_x^2 + c_y^2} L_y - 2a(\frac{\pi}{2}, \hat{x}))$ , i.e., the contribution from each corner with bisectors along the  $y$  axis. This gives  $a(\frac{\pi}{2}, \hat{y}) = 0.143702$ , which is (to at least six significant digits)  $a(\frac{\pi}{2}, \hat{x})$  for a mass ratio  $m_x/m_y = 2$ .

## V. TIP-TOUCHING CORNERS

Until now, we have studied geometries for which the corner contribution to the EE is additive [see Eq. (2)]. One instance

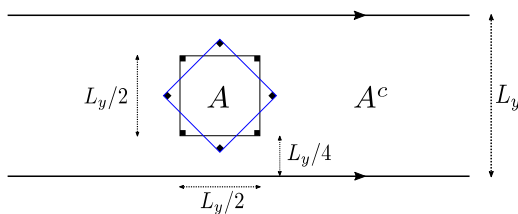


FIG. 13. Square subregions  $A$  and their complement on an infinite cylinder of circumference  $L_y$ : the black square is aligned with the  $x$  and  $y$  axes, while the blue one is rotated by  $\pi/4$ . In the presence of mass anisotropy, they give different entanglement entropies.

where this additivity fails is when two or more corners touch at their tip. As an example, consider the von Neumann EE in the  $\nu = 1$  state for the “hourglass” geometry in Fig. 14. We find that  $\gamma \neq 4a(\pi/2)$ , but that the contribution from the two touching corners (the other two are simply the bulk corners studied above), which we denote by  $a_x(\pi/2)$ , is

$$a_x(\pi/2) = \gamma - 2a(\pi/2) = 0.379024 > 2a(\pi/2), \quad (16)$$

where  $2a(\pi/2) = 0.170997$ . In fact,  $a_x(\pi/2)$  is close (but not equal) to *four* times the  $\pi/2$  contribution  $4a(\pi/2)$ . This clearly shows the failure of the additivity for touching corners. We have also obtained the result for the second Rényi entropy  $\alpha = 2$ :  $a_{x,2}(\pi/2) = \gamma_2 - 2a_2(\pi/2) = 0.232144 > 2a_2(\pi/2)$ .

For this geometry, it is of interest to compute the mutual information  $I(A_1, A_2) = S(A_1) + S(A_2) - S(A_1 \cup A_2)$ , where  $A_{1,2}$  are two subregions. Here, we take  $A_1$  to be the top part of the hourglass, and  $A_2$  the bottom part. We can make a simplification by ignoring what happens far from the point where the two corners meet. This could be achieved by working with an infinite hourglass embedded in the plane, or by making the vertical extent of the hourglass smaller than  $L_y$  and smoothing out the bulk corners so that the hourglass is the only singularity. In that case, we get the following mutual information:

$$I(A_1, A_2) = a_x(\pi/2) - 2a(\pi/2) = 0.208027. \quad (17)$$

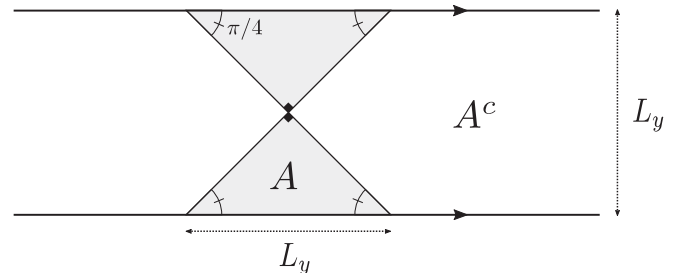


FIG. 14. “Hourglass” subregion  $A$  and its complement on an infinite cylinder of circumference  $L_y$ . Note that  $A$  contains four  $\pi/2$  corners, two of which touch at their vertex.

The boundary-law part canceled out, and we are left with an expression independent of all scales. Further, by the sub-additivity of the EE, we have that the mutual information is non-negative so that  $a_{\times}(\pi/2) \geq 2a(\pi/2)$ . Our numerical result is clearly consistent with this constraint.

## VI. CONCLUSION

We have studied the properties of the reduced density matrix for various regions with sharp corners in three IQH states: two ground states at fillings  $\nu = 1, 2$  and one excited state with the first LL entirely full (and the zeroth and other LLs empty). We have studied the nontrivial angle dependence of the EE (and its Rényi generalizations), which is encapsulated by the corner function  $a(\theta)$ . This function is independent of all scales, including the magnetic length  $\ell_B$ . Most strikingly, we found that the Hall corner function, when properly normalized, has a surprisingly close angle dependence to the corner function found in two-dimensional CFTs, as shown in Fig. 1. This superuniversality of the EE hints at common structures in very different quantum many-body states. In particular, as we discussed in Sec. III C, the Hall corner terms obey bounds that hold for CFTs. It would be desirable to understand the reason for these common properties. In this regard, quantum information-theoretic concepts could reveal general properties about the entanglement structure of a large class of quantum many-body states.

We also examined the role of mass anisotropy on the EE, and showed that it strongly affects the shape dependence of the EE. We studied a different type of corner where two tips touch at a point (hourglass), and we were able to extract a universal quantity via the mutual information.

Going beyond the EE, we studied the entanglement spectrum, as well as the eigenfunctions of the reduced density matrix. In particular, we described how the eigenfunctions associated with low pseudoenergy eigenstates localize near sharp corners. The behavior of the entanglement spectrum also shows clear differences between the ground and excited states.

### Outlook

In this work, we have shown that IQH states provide a rich playground to study the entanglement structure of quantum states. The states we have studied are particularly simple, but nevertheless share common properties with much more complicated states such as the ground states of interacting two-dimensional CFTs. It would be of interest to study the same quantities in more intricate topological states, such as the Laughlin FQH states. For instance, it would be desirable to obtain the corner function  $a(\theta)$  for such FQH states, and compare its angle dependence with that of IQH states, and two-dimensional CFTs. This is a challenging task owing to the non-Gaussian nature of FQH states, but one could make use of the recent advances in representing trial wave functions using matrix product states (MPS) [37,38]. In particular, the MPS representation works for the infinite cylinder geometry used in this work. Apart from the numerical analysis, analytical results could be obtained, in particular in the nearly smooth

limit  $\theta \approx \pi$ , where analytical results already exist for general CFTs [13,14].

In the context of two-dimensional CFTs, it was recently realized that the EE of a region that intersects a physical edge of the system has a relation to the EE of a bulk region obtained by taking the union of the initial region and its mirror image about the edge [39]. This relation was shown to hold approximately for the IQH ground state at  $\nu = 1$  for a large range of intersection angles, and exactly for a specific angle [31]. It would be desirable to study this relation in the other IQH states studied in this work, as well as in FQH states.

## ACKNOWLEDGMENTS

We thank G. Sierra for sharing with us many results, both published and unpublished, on entanglement in quantum Hall states. We also thank C. Berthiere, A. Gromov, F. D. M. Haldane, L. Santos, P.-G. Rozon for useful discussions. This project was funded by a grant from Fondation Courtois, a Discovery Grant from NSERC, a Canada Research Chair, and a ‘‘Etablissement de nouveaux chercheurs et de nouvelles chercheuses universitaires’’ grant from FRQNT. B.S. was supported by an NSERC Undergraduate Student Research Award (USRA) and a FRQNT BIX Master’s scholarship. L.M.F. was supported by a NSERC Undergraduate Student Research Award (USRA) and a NSERC Master’s Scholarship. This work was initiated and partially performed at the Aspen Center for Physics, which is supported by National Science Foundation Grant No. PHY-1066293.

## APPENDIX A: NUMERICAL VALUES

We give the numerically calculated corner function  $a_{\alpha}(\theta)$  in Table II, where  $\alpha$  is the Rényi index. According to our analysis, described in detail in Appendix B, all the quoted digits are numerically stable.

## APPENDIX B: PRECISION

The EE results from the diagonalization of the infinite-dimensional matrix  $\mathcal{F}(A)$ . To perform numerical computations, we had to truncate this matrix by ignoring terms related to electrons located further from the entanglement cut. These electrons contribute less to the EE, and are associated with high absolute value of the momentum  $k$ . In addition to the size of the matrix, it was necessary to consider, for every computation, a sufficiently large value for the circumference of the cylinder  $L_y$ . Indeed, we needed to consider a cylinder that is big enough for the area law to hold. The method implemented to ensure the convergence of the corner function of the von Neumann EE  $S(A)$  for any of the three states is the following. Concretely, for a desired precision  $\sim\delta$  on a value of the corner function  $a(\theta)$  (for a given angle  $\theta$ ), we first need to fix  $L_y$  and compute the EE from a matrix whose dimension  $N$  increases until it is stable at a precision of  $\sim 2\delta$  [2 for the number of corners in our region, this way the precision on the (possibly erroneous) corner function extracted from this EE is  $\sim\delta$ ]. Then, we redo this step for a significantly larger  $L_y$ . From these two EEs, the value of the corner function is calculated and compared to determine whether we have

TABLE II. Numerical values of  $a_\alpha(\theta)$ .

$\theta$ (deg)	$\alpha = 1$			$\alpha = 2$		
	$\nu = 1$	Filled first LL	$\nu = 2$	$\nu = 1$	Filled first LL	$\nu = 2$
5	3.15235	8.29181	6.19120	2.19050	7.17506	4.41980
10	1.56134	4.09623	3.06824	1.08834	3.57006	2.19540
15	1.02634	2.68343	2.01796	0.717969	2.36081	1.44788
25	0.591423	1.53394	1.16366	0.416631	1.38026	0.839960
35	0.399602	1.02778	0.786566	0.283233	0.947825	0.570982
45	0.289663	0.739082	0.570368	0.206366	0.698379	0.415970
55	0.217535	0.550975	0.428509	0.155638	0.532717	0.313651
65	0.166224	0.418217	0.327573	0.119344	0.412985	0.240445
75	0.127776	0.319567	0.251913	0.0920046	0.321673	0.185314
85	0.0979695	0.243721	0.193228	0.0707108	0.249586	0.142389
90	0.0854987	0.212181	0.168664	0.0617735	0.219010	0.124377
95	0.0743545	0.184105	0.146707	0.0537720	0.191448	0.108255
105	0.0554144	0.136645	0.109373	0.0401398	0.144027	0.0807942
115	0.0401632	0.0986867	0.0792945	0.0291311	0.105244	0.0586257
125	0.0279366	0.0684378	0.0551689	0.0202846	0.0737173	0.0408167
135	0.0182760	0.0446606	0.0360985	0.0132814	0.0485057	0.0267218
145	0.0108613	0.0264893	0.0214566	0.00789824	0.0289604	0.0158896
155	0.00547020	0.0133214	0.0108077	0.00397976	0.0146362	0.00800594
165	0.00195267	0.00475064	0.00385825	0.00142108	0.00523667	0.00285860
170	0.000865582	0.00210523	0.00171033	0.000629997	0.00232299	0.00126727
175	0.000216057	0.000525388	0.000426921	0.000157262	0.000580090	0.000316338

reached a sufficient  $L_y$  for the area-law (1) to hold. These two steps are then repeated until the precision on the corner function reaches  $\sim \delta$ . We note that the minimum dimension  $N$  for the EE convergence seems directly proportional to  $L_y$  and Fig. 15 shows the transition to the boundary-law regime for the von Neumann EE  $S(A)$  as a function of  $L_y$ , for multiple arrow-shaped subregions  $A$  of angles  $\theta$ .

Figure 16 shows an example of the minimal dimension  $N$  of  $\mathcal{F}(A)$  with a fixed  $L_y$  (big enough for the area-law regime) when  $\theta$  is far from the limits  $\theta \rightarrow 0$  and  $\theta \rightarrow \pi$ , for the  $\nu = 1$

state. As we can see, the minimal dimension of the matrix seems to be directly proportional to  $\ell_x$ .

For reference, in calculating the corner function for the von Neumann EE at a precision of  $10^{-10}$ ,  $\frac{L_y}{\ell_B} \gtrsim 30$  was more than enough for all angles for the  $\nu = 1$  state. For the  $\nu = 2$  state, the required length was also  $\frac{L_y}{\ell_B} \gtrsim 30$  and for the first filled LL,  $\frac{L_y}{\ell_B} \gtrsim 35$ . Also, generally, smaller angles do not require as a big a minimal length: for the  $\nu = 1$  state,  $\frac{L_y}{\ell_B} \gtrsim 15$  was enough for  $\theta = 30^\circ$ , whereas  $\theta = 90^\circ$  and  $175^\circ$  required  $\frac{L_y}{\ell_B} \gtrsim 25$ .

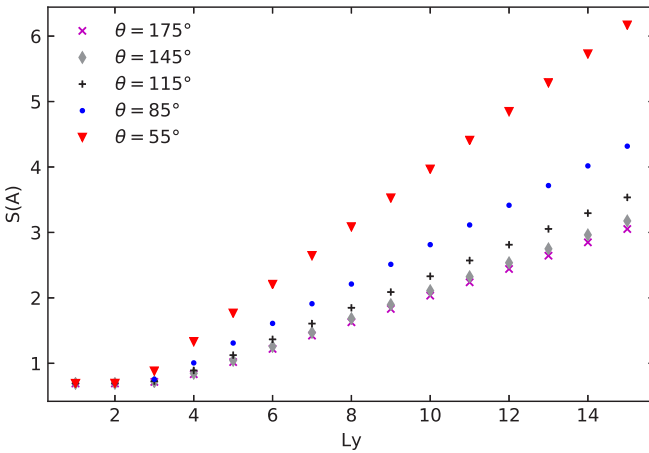


FIG. 15. Von Neumann EE as a function of cylinder circumference  $L_y$  for the  $\nu = 1$  ground state. We note the transition to the boundary-law regime for every arrow-shaped region of angles  $\theta$ . At large  $L_y$ , we recover the boundary law  $S(A) = c \frac{L_A}{\ell_B} - 2a(\theta) + \dots = c \csc\left(\frac{\theta}{2}\right) \frac{L_y}{\ell_B} - 2a(\theta) + \dots$ .

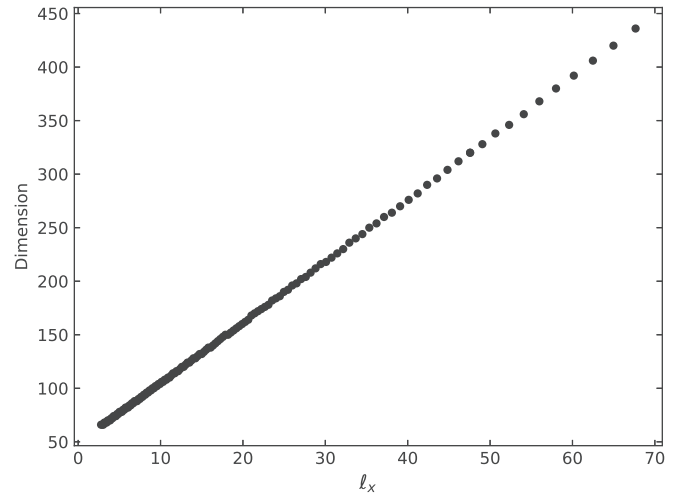


FIG. 16. Minimal dimension  $N$  of  $\mathcal{F}(A)$  [so that we consider  $k$  of quantum number  $m \in [-N/2 + 1, N/2]$  in  $\mathcal{F}(A)$ ] as a function of  $\ell_x$ , for a stable  $a(\theta)$  for the LLL state with a precision  $10^{-8}$  and where  $L_y = 30$ .

By and large, the results obtained for smaller angles have many more significant digits of precision, but require more computing power, as a bigger matrix is necessary to completely “define” the cut which is spatially larger than in the smooth limit. This is why we were not able to compute the corner function for very small angles ( $\theta \leq 0.035$ ). The results close to a smooth cut are much less precise. Indeed, the corner functions are small in that limit, quite close to machine preci-

sion. All computations in the large-angle limit were, however, much less demanding.

The precision of the constants for the asymptotic behavior near  $\pi$  was limited by the fitting of the ratio of two very small functions [ $a(\theta \rightarrow \pi)$  and  $(\theta - \pi)^2$ ], whereas the precision of constants for the asymptotic behavior at small angle was limited by the fact that we were not able to get data for the corner functions at very small angles.

- 
- [1] A. Kitaev and J. Preskill, *Phys. Rev. Lett.* **96**, 110404 (2006).  
 [2] M. Levin and X.-G. Wen, *Phys. Rev. Lett.* **96**, 110405 (2006).  
 [3] S. Dong, E. Fradkin, R. G. Leigh, and S. Nowling, *J. High Energy Phys.* **2008**, 016 (2008).  
 [4] H. Li and F. D. M. Haldane, *Phys. Rev. Lett.* **101**, 010504 (2008).  
 [5] E. Fradkin, *Field Theories of Condensed Matter Physics* (Cambridge University Press, Cambridge, 2013).  
 [6] E. Fradkin and J. E. Moore, *Phys. Rev. Lett.* **97**, 050404 (2006).  
 [7] S. N. Solodukhin, *Phys. Lett. B* **665**, 305 (2008).  
 [8] H. Casini and M. Huerta, *J. Phys. A: Math. Theor.* **42**, 504007 (2009).  
 [9] T. Nishioka, S. Ryu, and T. Takayanagi, *J. Phys. A: Math. Theor.* **42**, 504008 (2009).  
 [10] R. C. Myers and A. Sinha, *Phys. Rev. D* **82**, 046006 (2010).  
 [11] A. B. Kallin, K. Hyatt, R. R. P. Singh, and R. G. Melko, *Phys. Rev. Lett.* **110**, 135702 (2013).  
 [12] A. B. Kallin, E. M. Stoudenmire, P. Fendley, R. R. P. Singh, and R. G. Melko, *J. Stat. Mech.: Theory Exp.* **2014**, P06009 (2014).  
 [13] P. Bueno, R. C. Myers, and W. Witczak-Krempa, *J. High Energy Phys.* **2015**, 91 (2015).  
 [14] T. Faulkner, R. G. Leigh, and O. Parrikar, *J. High Energy Phys.* **2016**, 68 (2016).  
 [15] N. Laflorencie, *Phys. Rep.* **646**, 1 (2016).  
 [16] J. Helmes, L. E. Hayward Sierens, A. Chandran, W. Witczak-Krempa, and R. G. Melko, *Phys. Rev. B* **94**, 125142 (2016).  
 [17] X. Chen, W. Witczak-Krempa, T. Faulkner, and E. Fradkin, *J. Stat. Mech.: Theory Exp.* **4**, 043104 (2017).  
 [18] P. Bueno and W. Witczak-Krempa, *Phys. Rev. B* **93**, 045131 (2016).  
 [19] W. Witczak-Krempa, *Phys. Rev. B* **99**, 075138 (2019).  
 [20] T. Hirata and T. Takayanagi, *J. High Energy Phys.* **2007**, 042 (2007).  
 [21] E. M. Stoudenmire, P. Gustainis, R. Johal, S. Wessel, and R. G. Melko, *Phys. Rev. B* **90**, 235106 (2014).  
 [22] P. Bueno and R. C. Myers, *J. High Energy Phys.* **2015**, 68 (2015).  
 [23] S. Whitsitt, W. Witczak-Krempa, and S. Sachdev, *Phys. Rev. B* **95**, 045148 (2017).  
 [24] P. Bueno, H. Casini, and W. Witczak-Krempa, *J. High Energy Phys.* **2019**, 69 (2019).  
 [25] I. D. Rodríguez and G. Sierra, *J. Stat. Mech.: Theory Exp.* (2010) P12033.  
 [26] I. Peschel, *J. Phys. A: Math. Gen.* **36**, L205 (2003).  
 [27] M. Legner and T. Neupert, *Phys. Rev. B* **88**, 115114 (2013).  
 [28] I. D. Rodríguez and G. Sierra, *Phys. Rev. B* **80**, 153303 (2009).  
 [29] L. Charles and B. Estienne, *Commun. Math. Phys.* **376**, 521 (2019).  
 [30] D. Karabali, *Phys. Rev. D* **102**, 025016 (2020).  
 [31] P.-G. Rozon, P.-A. Bolteau, and W. Witczak-Krempa, *Phys. Rev. B* **102**, 155417 (2020).  
 [32] B. Estienne and J.-M. Stéphan, *Phys. Rev. B* **101**, 115136 (2020).  
 [33] B. Estienne, J.-M. Stéphan, and W. Witczak-Krempa, Cornering the universal shape of fluctuations, [arXiv:2102.06223](https://arxiv.org/abs/2102.06223).  
 [34] P. Bueno, R. C. Myers, and W. Witczak-Krempa, *Phys. Rev. Lett.* **115**, 021602 (2015).  
 [35] P. Calabrese and J. Cardy, *J. Stat. Mech.: Theory Exp.* **2004**, 06002 (2004).  
 [36] B. Yang, Z. Papić, E. H. Rezayi, R. N. Bhatt, and F. D. M. Haldane, *Phys. Rev. B* **85**, 165318 (2012).  
 [37] M. P. Zaletel and R. S. K. Mong, *Phys. Rev. B* **86**, 245305 (2012).  
 [38] B. Estienne, Z. Papić, N. Regnault, and B. A. Bernevig, *Phys. Rev. B* **87**, 161112(R) (2013).  
 [39] C. Berthiere and W. Witczak-Krempa, *Phys. Rev. B* **100**, 235112 (2019).